

# 1.5% root-mean-square flat-intensity laser beam formed using a binary-amplitude spatial light modulator

Jinyang Liang,<sup>1,\*</sup> Rudolph N. Kohn, Jr.,<sup>2</sup> Michael F. Becker,<sup>1</sup> and Daniel J. Heinzen<sup>2</sup>

<sup>1</sup>Department of Electrical and Computer Engineering, University of Texas at Austin, Austin, Texas 78712, USA

<sup>2</sup>Department of Physics, University of Texas at Austin, Austin, Texas 78712, USA

\*Corresponding author: jinyang.liang@mail.utexas.edu

Received 8 December 2008; revised 10 March 2009; accepted 20 March 2009;  
posted 20 March 2009 (Doc. ID 104896); published 27 March 2009

We demonstrate a digital micromirror device (DMD)-based optical system that converts a spatially noisy quasi-Gaussian to an eighth-order super-Lorentzian flat-top beam. We use an error-diffusion algorithm to design the binary pattern for the Texas Instruments DLP device. Following the DMD, a telescope with a pinhole low-pass filters the beam and scales it to the desired sized image. Experimental measurements show a 1% root-mean-square (RMS) flatness over a diameter of 0.28 mm in the center of the flat-top beam and better than 1.5% RMS flatness over its entire 1.43 mm diameter. The power conversion efficiency is 37%. We develop an alignment technique to ensure that the DMD pattern is correctly positioned on the incident beam. An interferometric measurement of the DMD surface flatness shows that phase uniformity is maintained in the output beam. Our approach is highly flexible and is able to produce not only flat-top beams with different parameters, but also any slowly varying target beam shape. It can be used to generate the homogeneous optical lattice required for Bose–Einstein condensate cold atom experiments. © 2009 Optical Society of America

OCIS codes: 140.3300, 070.6120.

## 1. Introduction

High-quality, flat-top laser beams are important in many areas of optics and optical physics. By flat-top, we mean a laser beam with a central region of uniform irradiance surrounded by a transition region to zero as radius increases. A top hat or perfect circle function (Circ function) profile might be ideal, but it is impractical to achieve. Thus, various shapes, such as higher-order Gaussian and Lorentzian functions or cosine tapers are used to achieve a transition region between the flat central region and zero irradiance within a finite spatial frequency bandwidth.

In optics, flat-top beam applications include laser welding, laser microfabrication, laser radar, laser scanning, laser fusion, and optical processing. In op-

tical physics, flat-top beams could improve the sensitivity of interferometric gravity wave detectors [1]. Ultracold atoms loaded into optical lattices have important applications, including optical lattice atomic clocks [2] and quantum emulation [3]. Optical lattices are formed by standing wave interference of single-mode laser beams, generally of a Gaussian transverse profile, and ultracold atoms are attracted to the intensity minima or maxima by the optical dipole force. In such cold atom applications, flat-top beams can lessen the undesirable effects of spatial inhomogeneities by creating an optical lattice in which the potential wells are of uniform depth.

Our objective is to create a well-controlled laser beam to form the standing wave optical lattice potential for ultracold atom experiments. In this case, achieving a high degree of flatness over the central region is of primary interest. The phase of the wave front is also important to establish a uniform optical

standing wave field; a uniform, flat phase front over the flat-top region is required. The transition region and wings of the beam are less important as the cold atoms never see this region and remain confined in the lowest potential region. Finally, in our application, we can sacrifice some degree of conversion efficiency from the input Gaussian profile beam to the desired profile in order to achieve a high degree of beam shape control and a minimum root-mean-square (RMS) deviation from the targeted beam shape. A conversion efficiency of 25%–50% with a peak power of 25%–50% of the input Gaussian beam is sufficient provided the other criteria are met. For cold atom experiments, an ultimate intensity flatness of the order of 0.1% RMS is desired. In the first step toward this goal, we want to get as close as possible to a 1% RMS error in a flat-top beam by using an accurate initial measurement of the input Gaussian beam and a good design algorithm for the beam shaper. This first step is the subject of this paper. For the future, one might consider refinement of the beam based on repeated measurements of the beam profile or of the cold atom distribution, which is even more sensitive to small variations in the optical field. For beam refinement, peaks could be suppressed and valleys lifted toward the mean to achieve a more accurate flattop.

A laser beam with homogeneous intensity can be generated through various approaches. Here, we briefly compare techniques that use transmissive optics (images of masks and masklike mirrors), refractive optics (lenses and aspheric elements), and diffractive optics (with propagation to a Fourier transform plane or to a near-field plane). Metal masks have been used in transmissive optical beam-shaping systems. One way to generate a flat-top beam is via serrated-tooth apodizers designed by relating serration dimensions and spatial filter parameters. Auerbach and Karpenko [4] reported a flat-top beam profile produced by a serrated-edge aperture followed by a spatial filter. Although this approach can produce a flat-top beam that is both flat in intensity and phase, it requires a known input intensity profile matched to the apodizer design. It is, of course, possible to make this technique adaptive by forming the serrated aperture by reflection from a DMD spatial light modulator (SLM). Later work by Dorrer and Zuegel [5] demonstrated the error-diffusion technique to design and simulate the performance of metal masks that formed the desired target beam profile in an image plane following a low-pass filter. Our design is derived from this method, and so it will be described in more detail in Section 3.

Hoffnagle and Jefferson [6] used a refractive optical system composed of two aspheric lenses to convert a collimated Gaussian beam into a flat-top beam. This method achieved 5% RMS intensity variation in a flat-top beam with 78% power conversion. The design has high power-conversion efficiency, is achromatic, and can achieve a flat output profile in

both intensity and phase. However, since the calculation of lens surfaces is based on specific input and output beam shapes, the whole system can only work well for the single input–output combination. In addition, the technique can do nothing to reduce the effect of spatial noise and imperfections present in real laser beams.

The use of diffractive optics and holographic optical elements is popular for producing arbitrary light distributions. The conversion of Gaussian beams using diffractive optical elements (DOEs) has been intensively studied for many years. However, these methods have drawbacks when used to produce flat-top beams with flat phase. This difficulty was addressed by Aleksoff *et al.* [7], who used two DOEs: the first to produce a near-field flat-top beam profile with nonflat phase and a second one to flatten the phase. Their result showed roughly 20% RMS variation in a square cross-section, flat-top beam and a near diffraction limited (but not ideally sinc-shaped) far-field spot, indicating good phase flatness.

Another diffractive approach is to use an annular-phase plate containing two or more zones with binary phase values (usually 0 and  $\pi$ ). Based on the original proposal by Veldkamp and Kastner [8], various schemes have been published to produce flat-top beams from an input Gaussian beam [9–12]. However, since this binary phase plate is centrosymmetric, the input Gaussian beam also needs to have a very good centrosymmetric Gaussian intensity profile. This requirement limits the application of the binary annular-phase optical element.

To achieve a design that is adaptable to arbitrary input and output beam shapes, iterative Fourier transform algorithms (IFTA) have been used to design patterns for phase-only SLMs (or for fixed phase plates) for beam shaping. In a recent improvement to these techniques, Pasienski and DeMarco [13] reported a new IFTA to create the square cross-section, flat-top intensity profile. Their result pushes intensity error to an unimportant region of the output plane and reduces the error in the measurement region. In their adaptation of the IFTA, intensity is constrained only in the measurement region of the output plane, and phase is unconstrained. In a simulated result for an ideal phase-only SLM, they reported an RMS error of 1.5% with a power conversion efficiency of 45%. No data for the phase flatness were given. In general, such solutions are designed for a phase-only SLM and thus are inherently an approximation to ideal phase and amplitude modulation for the DOE.

Good examples of flat-top beams of very wide diameter (as compared to the equivalent focused Gaussian) are those results that use an IFTA or analytic solution to generate a DOE having a large parabolic phase component [14–16]. Although there is discussion as to the best IFTA to use to produce the lowest intensity noise in a flattop [13], it is the unconstrained phase that has the most important effect on the performance of the flattop through focus.

The DOE is placed before or after a lens, and the flat-top is formed in the focal plane of the lens. In this case, the parabolic phase component of the DOE shifts the plane with the smallest focus spot away from the focal plane of the lens, while the flattop is formed at the focal plane of the lens. Thus, the flat-top is formed in a plane of misfocus of the combined optical system. The flattop contains a large parabolic wavefront curvature and either converges or diverges rapidly. Although wide and flat, this flat-top output would be unsatisfactory for any application where phase or depth of focus is important.

We have chosen the transmissive approach using a digital micromirror device (DMD), Texas Instruments (TI) Digital DLP SLM, with an imaging system containing a low-pass filter. This system is expected to give a reasonably uniform phase and can control the light transmission in a programmed way. Adapting the technique of Dorrer and Zuegel [5] and adding further iterative pattern refinement, we design a DMD reflectance function that will produce the required beam shape after spatial filtering. We begin with a discussion of our approach to making flat-top laser beams in Section 2. The SLM pattern design algorithm is described in Section 3, followed by the experimental results in Section 4. In Section 5, we compare our results to the performance of various other methods reported to produce flat-top beams with respect to intensity uniformity, phase flatness, and flexibility. A concluding summary follows in Section 6.

## 2. Approach to Making Flat-Top Laser Beams

The target flat-top function used in the work reported here is an eighth-order super-Lorentzian. Other functions have been tested in simulation only (eighth-order super-Gaussian and cosine taper similar to the eighth-order super-Lorentzian) and by generating a flat-top beam and measuring the flat-top profile (cosine taper). These tests, reported in Section 4, showed no significant difference in RMS flatness between functions that has a similar spatial frequency bandwidth. Generating flat-top beams based on different functions demonstrates the adaptability of our method, and that the differences between these functions of similar spatial bandwidth do not affect the quality of the flat-top beam produced.

Several factors need to be considered to make a high-quality flat-top beam. First, accurately measured profiles of the input beam and the output flat-top beam are necessary. Second, the DMD pattern and spatial filter need to be designed properly to produce the desired multiplicative reflectance curve shown in Fig. 1. Finally, the flat-top beam profile needs to be measured before fringes or dirty spots on optical components can degrade it. This implies a stringent requirement on optical quality and cleaning.

To produce and measure flat-top beams, we constructed a test bench consisting of a laser, a DMD

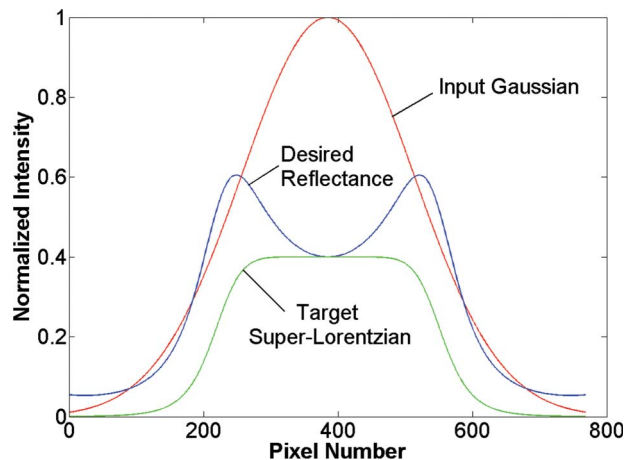


Fig. 1. (Color online) Cross sections of a simulated Gaussian input beam ( $r_G = 256$  pixels), an eighth-order super-Lorentzian (SL) beam ( $r_{SL} = r_G/1.5 = 171$  pixels), and the desired reflectance function,  $R$ , to transform one into the other. The beam profiles and  $R$  are defined in Eqs. (3) and (4).

SLM, and an imaging telescope with a spatial filter. The general layout of the test bench is shown in Fig. 2. The DMD was the TI Discovery 1100 platform with  $1024 \times 768$  pixels at a pitch of  $13.68 \mu\text{m}$ . The input beam from a He-Ne laser (approximately Gaussian) is expanded and collimated with a  $5\times$  telescope to best fit the DMD size ( $14 \times 10.5$  mm). No effort was made to clean up this beam or to ensure that its profile was accurately Gaussian. In the beam path to the DMD, a  $45^\circ$  mirror on a kinematic mount was inserted in order to form an equivalent plane to the DMD surface at the CCD camera face. The camera was placed at exactly the same distance from the mirror as the DMD. This ensured that the image captured by the camera was exactly the same as the one incident on the DMD. This image was sent to an algorithm that computed the binary reflectance function for the DMD. After the mirror was removed and the pattern written to the DMD, the beam reflected from the DMD and passed through a telescope with a low-pass filter (pinhole) at the back focal plane of the first lens. The output flat-top beam profile was measured at the output image plane of the telescope. We use the words “reflects” and “multiplicative reflection” to summarize the process of  $n$ th-order diffraction near the blaze angle of the DMD mirrors tilted to the ON state to produce the output beam.

To accurately measure the input and output beam profiles, we used the Scorpion SCOR-20SOM camera by Point Grey Research, Inc. that was prepared by Spiricon, Inc. to be windowless for accurate beam-profiling measurements with Spiricon laser beam diagnostic software. The Scorpion camera uses the Sony ICX274AL black and white CCD chip with  $4.4 \mu\text{m}$  square pixels in a  $1600 \times 1200$  array. The absence of the protective window minimizes fringes or diffraction patterns caused by parallel surfaces and dirty spots.

The ability to reduce camera artifacts enables us to measure high-quality beam profiles. At the laser

wavelength of 633 nm, the external quantum efficiency of the camera is 31% and the full-well capacity for each pixel is 8000 electrons [17]. Thus, for measurements of the output flat-top beam at the 3100 digital number (DN) level, the photon noise is around 0.18% after 16-frame averaging. The improvement in SNR is proportional to the square root of the number of frames being averaged. The measured spatial gain noise matches the camera specification of 0.8%. In addition, the raw 12 bit image data (0 to 4095) are stored for each frame. Digitization at 12 bits has the ability to represent a detailed image and reduce the digitization noise to a negligible level as compared to the other noise sources.

The way in which the flat-top laser beam is produced is based on binary DMD modulation plus imaging optics that includes a low-pass filter. The input Gaussian wave with the amplitude distribution  $g_1(x,y)$  is incident on the DMD, a binary SLM. The binary DMD pattern,  $DMD(x,y)$ , is determined by the measurement of the input beam and a two-step algorithm (details will be given in Section 3). Thus, after the DMD, the amplitude distribution of the  $n$ th-order diffracted light (nearest the blaze angle),  $g_2(x,y)$ , is given by

$$g_2(x,y) = g_1(x,y) \times DMD(x,y). \quad (1)$$

In the imaging telescope, the Fourier transform of the wave leaving the DMD surface is formed in the back focal plane of the first lens. A pinhole placed at this Fourier plane serves as a low-pass filter. The amplitude distribution in the frequency domain after the pinhole is given by

$$g_3(f_x, f_y) = F\{g_2(x,y)\} \times h(f_x, f_y), \quad (2)$$

where  $F\{\}$  represents the Fourier transform operator and  $h(f_x, f_y)$  is the binary-amplitude transmission of the pinhole. At the output plane, the light intensity distribution is the magnitude squared of the Fourier transform of  $g_3(f_x, f_y)$ . By proper control of the DMD pattern and the radius of the pinhole, a flat-top laser beam can be generated.

After designing the DMD pattern, it is important that the input Gaussian beam be aligned exactly on top of the DMD pattern (in  $x$ ,  $y$ , and rotation). In the optical setup, a shadow mask is placed in front of the diverting mirror to acquire an additional image of the incident Gaussian beam with the shadow mask

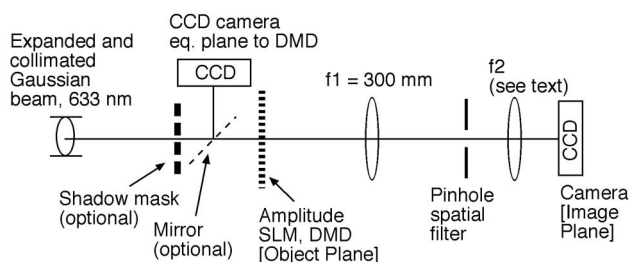


Fig. 2. Flat-top laser beam optical test bench configuration.

inserted, as shown in Fig. 2. The shadow mask needs to have as fine a pattern as possible without being totally destroyed by diffraction. Therefore, a trade-off needs to be made. In the experiment, we used a three-bar pattern ( $0.5\text{ mm} \times 2.5\text{ mm}$  each with a  $0.5\text{ mm}$  space) from the Air Force resolution chart (Group 0, Element 1) or a circular hole array (diameter =  $2\text{ mm}$  and pitch =  $2.4\text{ mm}$ ).

The picture with the shadow mask is processed to create a binary digitized image of the shadow mask. This pattern is input to the DMD to facilitate the  $x$ ,  $y$ , and rotation adjustment of the DMD with respect to the incident beam. The first lens in the imaging telescope focuses the modulated light into an optical power meter. This intensity represents the cross correlation of the input Gaussian containing the shadow mask pattern with the binary DMD pattern of the same shadow mask. The position of the DMD is adjusted for maximum power that is the peak of the cross correlation and correct alignment position. After the flat-top beam is generated, final adjustment of  $x$  and  $y$  is conducted by monitoring the RMS error in the flat-top region by using Spiricon laser beam diagnostics software to achieve the lowest RMS variation.

### 3. DMD Pattern Design Algorithm

The binary DMD pattern is designed by an error-diffusion algorithm followed by iterative refinement. A flow chart of our algorithm is shown in Fig. 3. The basic error-diffusion algorithm is based on that used by Dorrer and Zuegel [5]. Their design approach is suitable for binary pixelated beam shapers using DMD SLMs. First, the input Gaussian is captured at the equivalent plane to the DMD. The target function is an eighth-order super-Lorentzian,  $SL(x,y)$ , whose width and height are referred to the input Gaussian and given by

$$G_1(x,y) = G_o \exp\left[\frac{2r^2}{r_G^2}\right], \quad (3)$$

$$SL(x,y) = SL_o \left[1 + \left|\frac{r}{r_{SL}}\right|^8\right]^{-1},$$

where  $r_{SL} = r_G/1.5$  and  $SL_o = 0.4G_o$ . These parameters give a target function that does not approach the Gaussian too closely, and the reflectance function

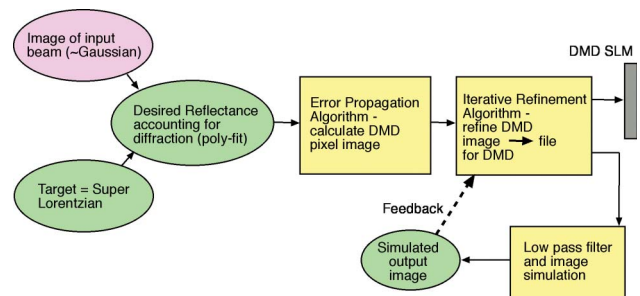


Fig. 3. (Color online) DMD pattern design algorithm flowchart.

does not become too sharply peaked or approach 1.0 (see Fig. 1). An increase in RMS error was observed when this limit was approached too closely.

Based on the input Gaussian and target super-Lorentzian functions, the desired reflectance function is calculated by

$$R_1(x,y) = SL(x,y)/G_1(x,y). \quad (4)$$

This is illustrated in Fig. 1 for  $r_G = N/3 = 256$  pixels and  $r_{SL} = r_G/1.5$ , where  $N = 768$ . The desired amplitude reflectance,  $r_1 = \sqrt{R_1(x,y)}$ , is then processed by the error-diffusion algorithm to produce the binary pixelated DMD pattern by rastering from left to right in a row and then from top to bottom in successive rows. Specifically, the binary value of  $DMD(x,y)$  is determined by comparing the desired amplitude reflectance  $r_1(x,y)$  modified by the propagated errors from nearby pixels that have already been processed to the threshold value of 0.5. The error function is calculated by

$$e(x,y) = r_1(x,y) - DMD(x,y), \quad (5)$$

and the reflectance function is replaced by

$$r_1(x+a,y+b) = r_1(x,y) + c(a,b) \times e(x,y), \quad (6)$$

where  $a$  and  $b$  are row and column coordinate shifts of the nearest neighbor pixels yet to be processed. The weighting coefficients for the four nearest neighbors are given by

$$\begin{aligned} c(1,-1) &= -3/16, & c(1,0) &= -5/16, \\ c(1,1) &= -1/16, & \text{and } c(0,1) &= -7/16. \end{aligned} \quad (7)$$

An iterative algorithm follows the error-diffusion algorithm to refine the DMD reflectance. The local peak of the simulated flattop (low-pass filtered) is found and the corresponding neighboring pixel, usually  $(x,y+1)$ , on the DMD pattern is set to zero. Fewer than 20 iterations are needed to converge, and the RMS error was typically reduced by 10%–30%. For an optimized error-diffusion algorithm, the RMS error over the simulated flattop was 0.2% to 0.3% for a 180 pixel diameter disk centered on the flattop (see Fig. 1). Interestingly, setting the  $(x,y)$  pixel to zero did not perform as well. This RMS error is due to the DMD pattern and its binary-amplitude pixels and will be referred to as the pixel-setting error. In their simulation results using only error diffusion, Dorrer and Zuegel [5] reported a peak error of 2.4% and a RMS error of 0.7% for a somewhat different target function, which was low and flat in the center with peaks near the edges.

We tried several other methods to generate the DMD pattern, but none performed as well as error diffusion without iterative correction. Repeating Dorrer and Zuegel, we tried a random dither algorithm. Compared to the error-diffusion method, the

random dither algorithm produced much worse results (RMS error = 3%). Second, electronic screen methods were used to synthesize the DMD pattern. The high spatial frequency content of the DMD was not needed to form a smooth flattop and so a large unit cell could be used without loss of resolution in the flat-top beam. Two cases were tried with unit cells of 17 and 37 pixels. Each unit cell had 18 or 38 equally distributed thresholds, respectively. The 17 pixel unit cell method is described by Stoffel and Moreland [18], and we extended this method to a 37 pixel unit cell. The unit cells continuously tile the surface of the DMD. The best electronic screen results had RMS errors 1.5 to 2 times larger than error diffusion without iterative refinement.

Finally, we note that the optical power conversion efficiency from Gaussian beam to flat-top beam using our method is dependent on the parameters of the super-Lorentzian with respect to the input Gaussian. Coincidentally, for the parameters chosen,  $r_{SL} = r_G/1.5$  and  $SL_o = 0.4G_o$ , the power contained in the flattop is 40% of the input power, virtually identical to the reduction in the peak power. Conducting the same efficiency calculation for our experimental input beam, we obtained a power efficiency of 37%. For a top-hat beam profile, the maximum possible power conversion efficiency from a Gaussian input beam is 39% at a peak power conversion of 60%. Other target beam profiles, such as a super-Lorentzian or super-Gaussian, achieve higher power-conversion efficiency, but the extra converted power is located in the wings of the distribution and not useful for most applications. However, this energy is useful in reducing diffraction at high angles that would result from sharp edges in the light distribution.

#### 4. Experimental Results

Based on the design and simulation results shown above, we conducted experiments to produce a flattop and measure its quality. The imaging telescope had a magnification of  $-5/6$  and used 300 and 250 mm focal length lenses for  $f_1$  and  $f_2$ , respectively. This magnification was chosen in part to ensure that both the input and output beam profiles could be measured without camera saturation and without changing attenuators in the beam path. We observed that any change in optics, such as adding or removing attenuators, made the flat-top result worse because the measured incident beam was not precisely the same as the one incident on the DMD. A range of pinhole diameters was used (from 450 to 650  $\mu\text{m}$  in steps of 50  $\mu\text{m}$ ). Data are presented for the 500  $\mu\text{m}$  pinhole as it gave the best results.

Based on diffraction analysis, the power delivered to the desired diffraction order by the DMD device should scale as the square of the number of pixels set to the ON state. This was verified by applying the error-diffusion algorithm for a uniform input value of  $r$ . Using an optical power meter placed at the focal plane of the first lens (at the desired diffraction order), a series of optical power values were mea-

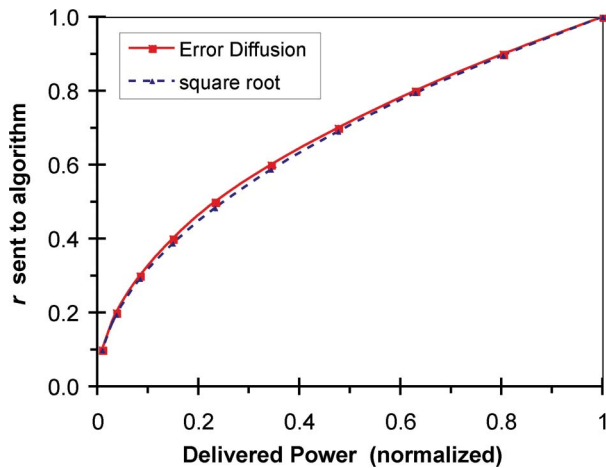


Fig. 4. (Color online) Plot of the uniform amplitude reflectance sent to the error-diffusion algorithm (fraction of DMD mirrors to be turned ON) versus the power delivered to the desired diffraction order (■) and the calculated square root of the delivered power (▲).

sured corresponding to  $r$  set from 0.1 to 1.0 in steps of 0.1. The measured power was normalized to one for  $r = 1$ , all pixels ON. The data are shown in Fig. 4 along with a square-root dependence. This confirms the use of  $r_1 = \sqrt{R_1(x, y)}$  in the DMD pattern design algorithm. For the experiments, a polynomial fit to the measured data was used to convert the desired diffracted power,  $R$ , into an amplitude reflectance,  $r$ , to send to the DMD pattern design algorithm.

The input laser beam was not spatially filtered. Its cross section and image are shown in Fig. 5. The experimental results (see Table 1) show that this noisy quasi-Gaussian input beam was transformed to a flat-top beam having RMS flatness of  $<1\%$  over a diameter of 64 camera pixels (0.28 mm) and  $<1.5\%$  over the entire output beam of 1.43 mm diameter. This result is illustrated graphically in Fig. 6(a), where the diameters of flat-top regions of a specified RMS error are shown superimposed on the cross section through the flat-top beam image.

To show the effect of the pinhole spatial filter, a 5.5 mm diameter pinhole was substituted for the 0.5 mm pinhole. In Fig. 6(b) the resulting noisy flat-top cross section is superimposed on the target super-Lorentzian function. Although noisy, the ragged unfiltered beam profile is, on average, flat and follows the target function. Figure 6(c) shows spatial frequency cross sections of the numerical two-dimensional Fourier transform of the target super-Lorentzian and the two experimental results with 5.5 and 0.5 mm pinholes. The spectrum for the optimum 0.5 mm pinhole is seen to follow the spectrum of the super-Lorentzian down to about 40 db below the peak value. For the 5.5 mm pinhole,

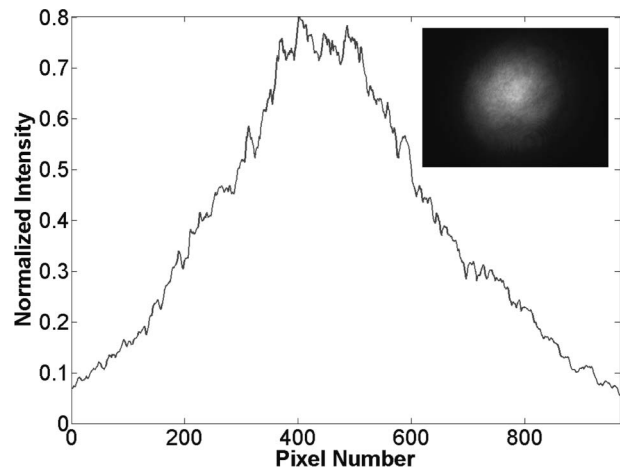


Fig. 5. Vertical cross section of the measured quasi-Gaussian input beam and its gray-scale image (inset). The horizontal axis is scaled by 5/6 to match the scale of the output plane images in Fig. 6. Each camera pixel is  $4.4 \mu\text{m}$ , and the  $1/e^2$  beam waist at the output is  $r_G \sim 420$  pixels = 1.85 mm.

the larger high-frequency content is visible out to the cutoff frequency of this larger pinhole. These plots clearly illustrate the function of the low-pass filter in converting the binary output from the DMD into a smooth flat-top beam profile.

Briefly we review the results of tests with other spatial profiles. The eighth-order super-Gaussian function with the same radius as the super-Lorentzian was visibly sharper in the wings, had a larger spatial bandwidth, and had three times larger RMS error when a DMD pattern was designed and simulated. Lower-order Gaussian functions with spatial bandwidth similar to the eighth-order super-Lorentzian were deemed insufficiently flat in the center region. A cosine taper similar to the super-Lorentzian was designed and tested optically. It had a central flat region (Circ function) of radius  $r_{\text{cos}} = r_G/2.8 = 0.5357r_{\text{SL}}$  and a taper width (one-half of the cosine period) of  $\Delta r = 2r_{\text{cos}}$ . Its measured RMS flatness was indistinguishable from that of the eighth-order super-Lorentzian flattop ( $<3\%$  different at all measurement points). Thus, the cosine taper may be more practical for applications requiring that the flat-top function go to zero within a prescribed radius.

## 5. Analysis and Discussion

In addition to an intensity flatness of better than 1.5% RMS, we also assessed the phase flatness of our flat-top beam. Three factors enter into the evaluation of the phase flatness of flat-top beams generated by our method. First, a  $5\times$  telescope is used to expand and collimate the Gaussian beam from the

Table 1. Measured RMS Flatness of the Output Flat-Top Beam

Diameter (pixel)	64	126	196	286	310	324
Diameter (mm)	0.282	0.554	0.862	1.258	1.364	1.426
RMS error (%)	1.0	1.1	1.2	1.3	1.4	1.5

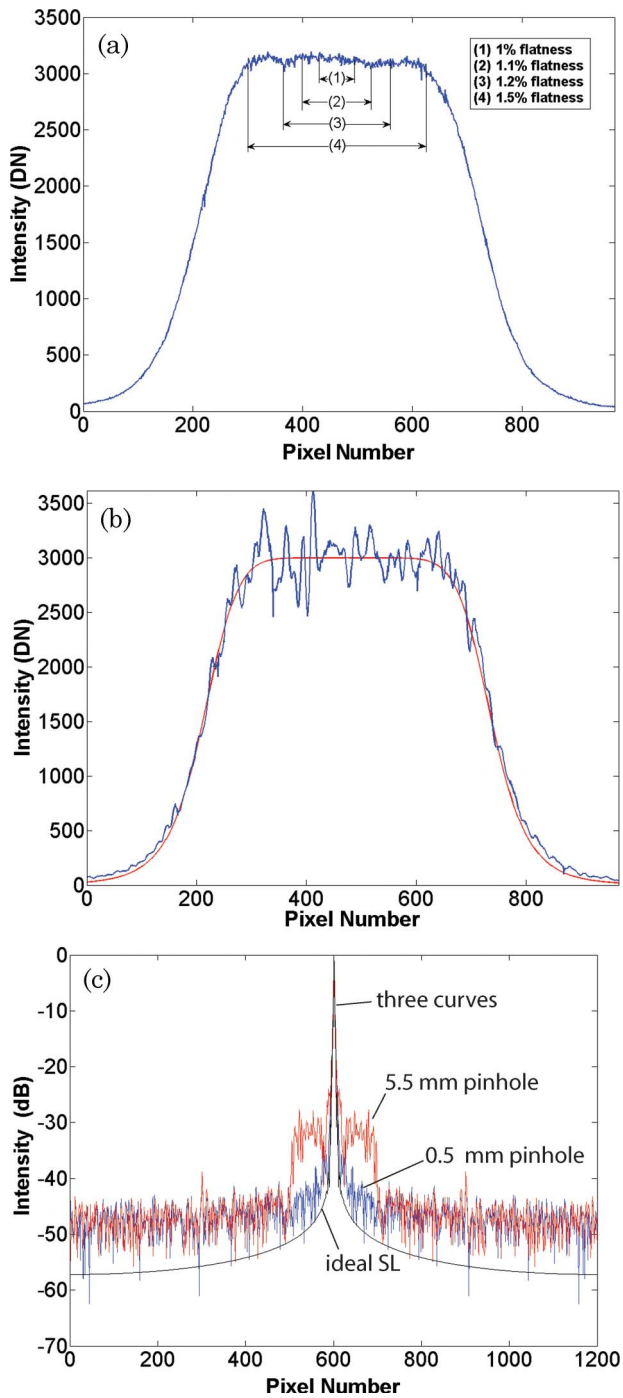


Fig. 6. (Color online) (a) Cross section of the experimental flat-top laser beam with a  $500\text{ }\mu\text{m}$  pinhole. (b) Experimental cross section with a  $5.5\text{ mm}$  pinhole compared to the ideal super-Lorentzian profile. (c) Spatial frequency spectra of the target super-Lorentzian, the experimental flat-top beam with a  $500\text{ }\mu\text{m}$  pinhole, and the experimental beam with a  $5.5\text{ mm}$  pinhole. In (a) and (b), each camera pixel is  $4.4\text{ }\mu\text{m}$ , while in (c) the pixel number represents spatial frequency from a 1200-point Fourier transform of the flat-top image ( $200\text{ pixels} = 38\text{ lp/mm}$  and zero frequency is at pixel number 600).

laser. The collimation of this beam ensures a flat phase front for the input beam at the DMD face.

Second, the DMD face flatness was measured using the Michelson interferometer. Many SLMs based on silicon chip technology possess a curvature

that has a quadratic or spherical component (that can be compensated by refocusing) and other aberrations, especially astigmatism. The DMD modulator that we used had a variation of three fringes (at  $633\text{ nm}$ ) from center to edge in the short dimension, and 8 to 10 fringes from center to edge in the long dimension and was astigmatic. Fortunately, the central portion that controlled the flat portion of the flat-top beam was very uniform in phase. In this area, the maximum-to-minimum phase difference in both the vertical and horizontal directions was measured. The result showed that, in the horizontal direction, the phase difference was  $0.77\pi$  ( $0.12\text{ }\mu\text{m}$  in surface height). In the vertical direction, the phase difference was  $0.16\pi$  ( $0.025\text{ }\mu\text{m}$  in surface height). Excellent DMD face flatness over this region is an important prerequisite to produce an output beam profile with good phase flatness.

Finally, the use of a telescope to image the wavefront leaving the DMD face to the output plane (with low-pass filtering) ensures that the phase flatness of the output is of the same quality as the wave leaving the DMD face. Thus, the uniform output phase front is another attractive advantage of this method of flat-top beam production.

When compared with the other methods outlined in Section 1, refractive optics has produced 5% RMS flatness using aspheric lenses [6] with, in principle, a well-controlled phase. The result is dependent on the quality of the input Gaussian beam. Although easy to use once the aspheric telescope is constructed, flexibility and adjustability are limited. In simulations, an IFTA algorithm produced 1.5% RMS flatness over the flat-top region [13]. However, the phase of the output was not controlled by the iterative routine and its behavior was not presented in the results. Furthermore, an experimental test with a phase-only SLM was not conducted, so a direct comparison of experimental results is not possible. Finally, as noted earlier, an approach similar to ours that used only error diffusion to design a metal mask followed by a low-pass filter showed simulated beam shaping with RMS error = 0.7% [5]. Our method has produced a lower RMS error than other reported methods, preserved the uniform phase of the wavefront, and delivered a power conversion efficiency of nearly 40%. Thus, it meets the criteria set forth for the first step in producing a flat-top beam suitable for uniform-lattice, cold atom experiments.

We note that there exists a gap between the best experimentally measured flatness of 1.4% RMS (for diameter = 310 camera pixels) and the simulated flatness for the same DMD pattern of 0.3%. Accounting for the sum of the major known errors, one expects the RMS error in a camera measurement to be the sum of the photon noise ( $<0.2\%$ ), spatial gain noise (0.8%), and DMD pixel-setting error (0.3%), giving a total expected RMS noise of 0.88%. Thus, there is a residual error in the flat-top beam of about 1.1% RMS. Although, alignment of the input Gaussian with the DMD was done while observing the beam's

RMS flatness in real time, the experimental flatness could not be further reduced. For future work, we propose to employ DMD pattern refinement based on the recorded output image to further improve the uniformity of the resulting flat-top beam.

## 6. Summary

We have demonstrated a DMD-based imaging optical system that converts a spatially noisy quasi-Gaussian to an eighth-order super-Lorentzian flat-top beam. An error-diffusion algorithm followed by iterative refinement was used to design the binary DMD pattern based on an accurate measurement of the beam incident on the DMD. Following the DMD, a telescope with a correctly sized pinhole low-pass filtered the flat-top beam and scaled it to the desired size. An alignment technique was developed to ensure that the DMD pattern was correctly positioned on the incident beam. Experimental measurements showed 1% RMS flatness over a diameter of 0.28 mm in the center of the flat-top beam and better than 1.5% RMS flatness over its entire 1.43 mm diameter. From an interferometric measurement of the DMD surface flatness in the critical portion of the flattop, we can infer phase uniformity better than  $0.8\pi$  across the output beam.

In comparison to other methods of generating flat-top beams, our approach shows the best result for RMS flatness with a good uniform phase front. Power conversion efficiency was 37%. In addition, our approach is highly flexible and is able to produce not only flat-top beams with different parameters, but also any slowly varying target beam shape.

The authors gratefully acknowledge the support of the Defense Advanced Research Projects Agency (DARPA) as a member of the Optical Lattice Emulator (OLE) initiative.

## References

1. M. G. Tarallo, J. Miller, J. Agresti, E. D'Ambrosio, R. DeSalvo, D. Forest, B. Lagrange, J. M. Mackowsky, C. Michel, J. L. Montorio, N. Morgado, L. Pinard, A. Remilleux, B. Simoni, and P. Willems, "Generation of a flat-top laser beam for gravitational wave detectors by means of a nonspherical Fabry-Perot resonator," *Appl. Opt.* **46**, 6648–6654 (2007).
2. M. Takamoto, F. L. Hong, R. Higashi, and H. Katori, "An optical lattice clock," *Nature* **435**, 321–324 (2005).
3. E. Jane, G. Vidal, W. Dur, P. Zoller, and J. I. Cirac, "Simulation of quantum dynamics with quantum optical systems," *Quantum Inf. Comput.* **3**, 15–37 (2003).
4. J. M. Auerbach and V. P. Karpenko, "Serrated-aperture apodizers for high-energy laser systems," *Appl. Opt.* **33**, 3179–3183 (1994).
5. C. Dorrer and J. D. Zuegel, "Design and analysis of binary beam shapers using error diffusion," *J. Opt. Soc. Am. B* **24**, 1268–1275 (2007).
6. J. A. Hoffnagle and C. M. Jefferson, "Design and performance of a refractive optical system that converts a Gaussian to a flattop beam," *Appl. Opt.* **39**, 5488–5499 (2000).
7. C. C. Aleksoff, K. K. Ellis, and B. D. Neagle, "Holographic conversion of a Gaussian-beam to a near-field uniform beam," *Opt. Eng.* **30**, 537–543 (1991).
8. W. B. Veldkamp and C. J. Kastner, "Beam profile shaping for laser radars that use detector arrays," *Appl. Opt.* **21**, 345–356 (1982).
9. R. de Saint Denis, N. Passilly, M. Laroche, T. Mohammed-Brahim, and K. Ait-Ameur, "Beam-shaping longitudinal range of a binary diffractive optical element," *Appl. Opt.* **45**, 8136–8141 (2006).
10. J. Jia, C. Zhou, X. Sun, and L. Liu, "Superresolution laser beam shaping," *Appl. Opt.* **43**, 2112–2117 (2004).
11. R. Bourouis, K. A. Ameur, and H. Ladjouze, "Optimization of the Gaussian beam flattening using a phase-plate," *J. Mod. Opt.* **44**, 1417–1427 (1997).
12. J. Cordingley, "Application of a binary diffractive optic for beam shaping in semiconductor processing by lasers," *Appl. Opt.* **32**, 2538–2542 (1993).
13. M. Pasienski and B. DeMarco, "A high-accuracy algorithm for designing arbitrary holographic atom traps," *Opt. Express* **16**, 2176–2190 (2008).
14. N. Sanner, N. Huot, E. Audouard, C. Larat, J. P. Huignard, and B. Loiseaux, "Programmable focal spot shaping of amplified femtosecond laser pulses," *Opt. Lett.* **30**, 1479–1481 (2005).
15. L. A. Romero and F. M. Dickey, "Lossless laser beam shaping," *J. Opt. Soc. Am. A* **13**, 751–760 (1996).
16. F. M. Dickey and S. C. Holswade, "Gaussian laser beam profile shaping," *Opt. Eng.* **35**, 3285–3295 (1996).
17. "A641f camera specification, measurement protocol using the EMVA Standard 1288" (Basler Vision Solutions AG, 2007).
18. J. C. Stoffel and J. F. Moreland, "A survey of electronic techniques for pictorial image reproduction," *IEEE Trans. Commun.* **29**, 1898–1925 (1981).